

A theoretical and computational framework for three dimensional inverse medium scattering using the linearized low-rank structure

Yuyuan Zhou^a, Lorenzo Audibert^b, Shixu Meng^c, and Bo Zhang^a

^aAcademy of Mathematics and Systems Science, Chinese Academy of Sciences, Beijing, 100190, China and School of Mathematical Sciences, University of Chinese Academy of Sciences, Beijing 100049, China

^bPRISME, EDF R&D, 6 Quai Watier, 78400 Chatou, France and UMA, Inria, ENSTA Paris, Institut Polytechnique de Paris, 91120 Palaiseau, France.

^cDepartment of Mathematical Sciences, The University of Texas at Dallas, 75025 Richardson, USA.

January 27, 2026

Abstract

In this work we propose a theoretical and computational framework for solving the three dimensional inverse medium scattering problem, based on a set of data-driven basis arising from the linearized problem. This set of data-driven basis consists of generalizations of prolate spheroidal wave functions to three dimensions (3D PSWFs), the main ingredients to explore a low-rank approximation of the inverse solution. We first establish the fundamentals of the inverse scattering analysis, including regularity in a customized Sobolev space and new a priori estimate. This is followed by a computational framework showcasing computing the 3D PSWFs and the low-rank approximation of the inverse solution. These results rely heavily on the fact that the 3D PSWFs are eigenfunctions of both a restricted Fourier integral operator and a Sturm-Liouville differential operator. Furthermore we propose a Tikhonov regularization method with a customized penalty norm and a localized imaging technique to image a targeting object despite the possible presence of its surroundings. Finally various numerical examples are provided to demonstrate the potential of the proposed method.

1 Introduction

Inverse scattering merits important applications in geophysical exploration, tunnel imaging, medical diagnosis, non-destructive testing and many others. It is a nonlinear and ill-posed problem, imposing challenges in both its analysis and inversion algorithm. Close to the study of this work, the linear sampling method [9] is a simple method for solving the inverse problem in the resonance region where Born approximation or physical optics is inadequate; it is worth mentioning other similar sampling methods, such as the factorization method [20], the generalized linear sampling method [3], and an alternative linear sampling method [2], among many others [15, 16, 18, 24, 25, 32]; for a more complete picture, we refer to the monographs [6, 7, 10, 22]. In a recent work [4] it was shown that, for a linear inverse problem, a formulation of the linear sampling method is capable of reconstructing the parameter, extending its shape reconstruction capability. The ill-posedness nature of inverse scattering has been elucidated in the work [21], showing that the ill-posedness of the inverse scattering problem is similar to the ill-posedness of its linearized (i.e. Born) approximation; the work [30] on inverse Born series demonstrated this property via a similar problem. To further shed light on the ill-posedness and to bridge the gap between data science and inverse scattering, the recent work [28] studied an intrinsic data-driven basis for the linearized inverse scattering problem and demonstrated a new explicit a priori estimate similar to the Holder-Logarithmic estimate [17]; such a set of data-driven basis naturally leads to a low-rank structure for a computational inversion technique [38], facilitating both computational

efficiency, robustness and a theoretical Lipschitz stability within a low-rank space. Such a linearized low-rank structure merits further application [8] in solving nonlinear inverse scattering problems in connection with the inverse Born series. The above-mentioned low-rank structure has been developed in two dimensions.

In this work we explore the low-rank structure for the three dimensional inverse scattering problem. Similar to the two dimensional case, the set of data-driven basis consists of generalization of prolate spheroidal wave functions to three dimensions [33], and we refer to such functions as 3D PSWFs in this work. Exploring the low-rank structure in three dimensions is a highly nontrivial study since both the analysis and the computation are more complicated. Our study depends heavily on the fact that the 3D PSWFs are eigenfunctions of both a restricted Fourier integral operator and a Sturm-Liouville differential operator, which is usually referred to as the dual property of PSWFs in the one dimensional case [31]. Taking full advantage of the dual property, this work contributes to the following: (1) establishing the fundamentals of the inverse scattering analysis, including a regularity estimate using the customized Sobolev space, a new a priori estimate similar to the Holder-Logarithmic estimate [17], and a new Lipschitz stability estimate in a low-rank space; (2) proposing a computational framework based on the low-rank structure given by a finite set of 3D PSWFs, sharing similar spirit to the singular value decomposition but facilitating robustness and efficiency thanks to a related Sturm-Liouville problem; (3) demonstrating a Tikhonov regularization method with a H_c^s penalty term (where H_c^s is a customized Sobolev space equivalent to the standard Sobolev space H^s) with a straightforward modification of the low-rank approximation; (4) facilitating a localized imaging technique (i.e., imaging targeting objects inside a ball when there are possible objects around) via the double orthogonality property of the 3D PSWFs (i.e., the 3D PSWFs are mutually orthogonal in both $L^2(\mathbb{R}^3)$ and the unit ball). As a next step, we plan to combine this linearized low-rank structure with other nonlinear inversion techniques to address more challenges. In a broader perspective, the low-rank structure is in the spirit of learning low dimensional features by machine learning [13, 36]; see recent machine learning approaches to inverse scattering, to name a few [11, 19, 23, 26, 29, 35, 39].

The remaining of the paper is organized as follows. In Section 2, we introduce the mathematical model of inverse scattering in three dimensions. Section 3 consists of various aspects of the analysis, including the introduction of the 3D PSWFs, the customized Sobolev space, the low-rank approximation with a priori estimate, the Tikhonov regularization method, and the localized imaging technique. Section 4 is mainly on the computational development, including computing the 3D PSWFs system and the approximate solution in the low-rank space. Finally various numerical experiments are conducted in Section 5, illustrating the full potential of the proposed low-rank structure.

2 Mathematical model of inverse scattering in three dimensions

Let $k > 0$ be the wave number and the contrast function $q(x) \in L^\infty(\Omega)$ be supported in an open and bounded set Ω . Without loss of Generality we assume that $\Omega \subset B(0, 1)$; here $B(0, 1) \subset \mathbb{R}^3$ is the unit ball. $\partial\Omega$ is assumed to be Lipschitz and $\mathbb{R}^3 \setminus \bar{\Omega}$ is connected. Let $u^i(x; \hat{\theta}; k) = e^{ikx \cdot \hat{\theta}}$ be a plane wave with incident direction $\hat{\theta} \in \mathbb{S}^2 := \{x \in \mathbb{R}^3 : |x| = 1\}$. In the context of acoustic scattering, the refractive index is related to $1 + q$ and the direct scattering due to the plane wave $u^i(x; \hat{\theta}; k) = e^{ikx \cdot \hat{\theta}}$ is to determine the total field $u^t \in H_{loc}^1(\mathbb{R}^3)$ such that

$$\begin{aligned} \Delta u^t + k^2(1 + q)u^t &= 0 \quad \text{in } \mathbb{R}^3, \\ u^t &= u^i + u^s, \\ \lim_{r:=|x| \rightarrow \infty} r \left(\frac{\partial u^s}{\partial r} - iku^s \right) &= 0. \end{aligned} \tag{1}$$

Here u^s represents the scattered wave field. A solution which satisfies the third equation, i.e., the Sommerfeld condition, uniformly for all directions $\hat{x} := x/|x| \in \mathbb{S}^2$ is called a radiating solution.

The above problem can be casted as the following problem to find a radiating solution $u^s \in H_{loc}^1(\mathbb{R}^3)$ to

$$\Delta u^s + k^2(1 + q)u^s = -k^2 q f, \tag{2}$$

where $f \in L^\infty(\mathbb{R}^3)$. To get the direct scattering problem (1), one simply sets f by $e^{ikx \cdot \hat{\theta}}$. According to [10], there exists a unique radiating solution to (1) and the solution satisfies the Lippmann-Schwinger integral

equation,

$$u^s(x; \hat{\theta}; k) = k^2 \int_{\mathbb{R}^3} \Phi(x, y)(u^s(y; \hat{\theta}; k) + e^{ik\hat{\theta} \cdot y})q(y)dy, \quad x \in \mathbb{R}^3,$$

where

$$\Phi(x, y) := \frac{1}{4\pi} \frac{e^{ik|x-y|}}{|x-y|}, \quad x \neq y,$$

is the fundamental function for the Helmholtz equation. The scattered field has the following asymptotic behavior (cf.[10])

$$u^s(x; \hat{\theta}; k) = \frac{e^{ikr}}{r} \left(u^\infty(\hat{x}; \hat{\theta}; k) + \mathcal{O}\left(\frac{1}{r}\right) \right) \text{ as } r = |x| \rightarrow \infty,$$

which holds uniformly with respect to all directions $\hat{x} = x/|x| \in \mathbb{S}^2$. It is known [10] that the far-field pattern can be represented by

$$u^\infty(\hat{x}; \hat{\theta}; k) = \frac{k^2}{4\pi} \int_{\mathbb{R}^3} e^{-ik\hat{x} \cdot y} \left(u^i(y; \hat{\theta}; k) + u^s(y; \hat{\theta}; k) \right) q(y) dy. \quad (3)$$

The multi-static data at a fixed frequency over the full aperture are given by

$$\{u^\infty(\hat{x}; \hat{\theta}; k) : \hat{x}, \hat{\theta} \in \mathbb{S}^2\}.$$

The inverse scattering problem is to determine the contrast q from these far field data. It is known that there exists a unique solution to this three dimensional inverse scattering problem, see [10]. In practical scenarios, far-field data is commonly encountered as a discrete dataset

$$\{u^\infty(\hat{x}_m; \hat{\theta}_\ell; k) : m = 1, 2, \dots, N_1, \ell = 1, 2, \dots, N_2\}.$$

The problem is nonlinear and severely ill-posed. Recent work [21] indicates that the eigenvalues of the data operator and these of its linearized version (i.e., Born data operator) decay at the same rate. Therefore, we are motivated to investigate the ill-posed nature of the Born model as a step towards the full model. The Born approximation $u_b^s(x; \hat{\theta}; k)$ is the unique radiating solution to the Born model

$$\Delta u_b^s + k^2 u_b^s = -k^2 q e^{ikx \cdot \hat{\theta}} \text{ in } \mathbb{R}^3. \quad (4)$$

Similarly, $u_b^s(x; \hat{\theta}; k)$ has the asymptotic behavior

$$u_b^s(x; \hat{\theta}; k) = \frac{e^{ikr}}{r} \left(u_b^\infty(\hat{x}; \hat{\theta}; k) + \mathcal{O}\left(\frac{1}{r}\right) \right) \text{ as } r = |x| \rightarrow \infty,$$

where the Born far field pattern is given by

$$u_b^\infty(\hat{x}; \hat{\theta}; k) = \frac{k^2}{4\pi} \int_{\mathbb{R}^3} e^{ik(\hat{\theta} - \hat{x}) \cdot y} q(y) dy. \quad (5)$$

The method of inverse Born series [30] can be applied where the key step is to understand the ill-posed Born inverse scattering problem (5); see [8] for the inverse Born series for solving inverse scattering with two unknown coefficients in two dimensions. We remark that we formulate the problem for a contrast in a unit ball; for a general contrast, it can be formulated via appropriate scaling, see for instance [28].

Loosely speaking, the formula (5) reveals that the Born far field pattern $u_b^\infty(\hat{x}; \hat{\theta}; k)$ is precisely the (scaled-) Fourier transform of contrast q evaluated only at $k(\hat{\theta} - \hat{x})$; the set of all possible $k(\hat{\theta} - \hat{x})$ leads to a ball of radius $2k$. Such a restricted Fourier integral operator leads to a data-driven basis for the inverse scattering problem in two dimensions [28]. A low-rank structure can be derived using a finite set of the basis functions, leading to a recent computational approach [38]. However it is highly non-trivial to generalize to the three dimensional case. In this work we aim to establish a theoretical and computational framework in three dimensions, with applications to Tikhonov regularization with customized penalty term and localized imaging.

Now we give the following formulation. Introduce $c = 2k$ and

$$u_b(p; c) := \frac{4\pi}{k^2} u_b^\infty(\hat{x}; \hat{\theta}; k) \quad \text{if} \quad p = \frac{\hat{\theta} - \hat{x}}{2}. \quad (6)$$

Since $\hat{x}, \hat{\theta} \in \mathbb{S}^2$, then it follows directly that $\{\frac{\hat{\theta} - \hat{x}}{2} : \hat{x}, \hat{\theta} \in \mathbb{S}^2\} = \overline{B}$ where B denotes the unit ball $B(0, 1)$. Note that even though there are many possible $(\hat{\theta}, \hat{x})$ which yield the same $p = \frac{\hat{\theta} - \hat{x}}{2} \in B$, however the value of $u_b(p; c)$ is uniquely determined due to (5). By a direct calculation, one verifies that

$$u_b(p; c) = \int_B e^{icp \cdot \tilde{p}} q(\tilde{p}) d\tilde{p}. \quad (7)$$

This is the formulation of the linearized inverse problem of reconstructing the unknown q from the processed data $u_b(p; c)$ given by (7). For the full model (2), the full far field data (with potential noise) $u^\infty(\hat{x}; \hat{\theta}; k)$ will lead to a perturbation u_b^δ such that $\|u_b^\delta - u_b\| \leq \delta$ for some perturbation level $\delta > 0$. We will demonstrate the a priori estimate and computational frameworks for general perturbed data u_b^δ .

3 A priori estimate and reconstruction formula

3.1 Generalization of prolate spheroidal wave functions

It is convenient to introduce the restricted Fourier integral operator $\mathcal{F}^c : L^2(B) \mapsto L^2(B)$ by

$$\mathcal{F}^c[g](x) = \int_B e^{icx \cdot y} g(y) dy, \quad x \in B,$$

where $c > 0$ is the bandwidth parameter. The prolate spheroidal wave functions were studied in a series of work [34, 33], and in particular [33] showed that the restricted Fourier integral operator is associated with the eigensystem $\{\psi_{m,n,l}(x; c), \alpha_{m,n}(c)\}_{m,n \in \mathbb{N}}^{l \in \mathbb{I}(m)}$ such that

$$\mathcal{F}^c[\psi_{m,n,l}](x) = \alpha_{m,n}(c) \psi_{m,n,l}(x; c), \quad (8)$$

where $\mathbb{N} = \{0, 1, 2, 3, \dots\}$ and $\mathbb{I}(m) = \{l \in \mathbb{Z} : |l| \leq m\}$. The eigenfunctions $\{\psi_{m,n,l}\}_{m,n \in \mathbb{N}}^{l \in \mathbb{I}(m)}$ are real-valued, analytical and form a complete orthogonal system of $L^2(B)$, and the eigenvalues $\{\alpha_{m,n}(c)\}$ satisfy following property,

$$\alpha_{m,n}(c) \rightarrow 0 \text{ as } m, n \rightarrow +\infty, \quad \text{and} \quad |\alpha_{m,n_1}(c)| > |\alpha_{m,n_2}(c)| > 0 \text{ for } n_1 > n_2.$$

The above eigensystem precisely leads to the data-driven basis $\{\psi_{m,n,l}(x; c)\}_{m,n \in \mathbb{N}}^{l \in \mathbb{I}(m)}$, and a low-rank structure can be formulated using a finite set of these basis functions. In this work the eigenfunctions are normalized such that

$$\int_{B(0,1)} \psi_{m,n,l}^2(y; c) dy = 1, \quad m, n \in \mathbb{N}, l \in \mathbb{I}(m).$$

From now on, we refer to the eigenfunction $\psi_{m,n,l}(x; c)$ as the 3D PSWF and the associated eigenvalue $\alpha_{m,n}(c)$ as the prolate eigenvalue.

One of the most important properties of the family of PSWFs is the so-called dual property [31]: the PSWFs are eigenfunctions of an integral operator and of a differential operator at the same time. In our case, the 3D PSWFs are also eigenfunctions of the following Sturm-Liouville differential operator such that

$$\mathcal{D}_c[\psi_{m,n,l}](x) = \chi_{m,n} \psi_{m,n,l}(x), \quad x \in B, \quad (9)$$

where \mathcal{D}_c in spherical coordinate (r, θ, ϕ) is given by

$$\mathcal{D}_c := -(1 - r^2) \partial_r^2 - \frac{2}{r} \partial_r + 4r \partial_r - \frac{1}{r^2} \Delta_{\mathbb{S}^2} + c^2 r^2$$

with the Laplace–Beltrami operator $\Delta_{\mathbb{S}^2}$ in spherical coordinate given by

$$\Delta_{\mathbb{S}^2} = \frac{1}{\sin \theta} \frac{\partial}{\partial \theta} \left(\sin \theta \frac{\partial}{\partial \theta} \right) + \frac{1}{\sin^2 \theta} \frac{\partial^2}{\partial \phi^2}.$$

Here with the spherical coordinate, one represents $x = (x_1, x_2, x_3)^T = r\hat{x}$ in cartesian coordinate by

$$x_1 = r \sin \theta \cos \phi, \quad x_2 = r \sin \theta \sin \phi, \quad x_3 = r \cos \theta.$$

The eigenvalue $\chi_{m,n}(c)$ will be referred to as the Sturm-Liouville eigenvalue and they are sorted according to $0 < \chi_{m,0}(c) < \chi_{m,1}(c) < \chi_{m,2}(c) < \dots$ for any $m = 0, 1, \dots$. The Sturm-Liouville eigenvalues approach to $+\infty$ in contrast to the prolate eigenvalues.

This dual property is due to the fact that the restricted Fourier integral operator \mathcal{F}_c and the Sturm-Liouville differential operator \mathcal{D}_c commutes with each other, i.e.,

$$\langle \mathcal{F}_c g, \mathcal{D}_c^* h \rangle = \langle \mathcal{D}_c g, \mathcal{F}_c^* h \rangle$$

for any pair of smooth functions g and h . The restricted Fourier integral operator \mathcal{F}_c , stemming from the inverse scattering problem, can be seen in the “main stage”; the seemly unrelated Sturm-Liouville differential operator \mathcal{D}_c , is the “backstage” hero in both the analysis and computation. More details about the family of PSWFs can be found in [14, 31, 33, 37]. In the following, we will demonstrate the theoretical and computational framework, using exactly the interplay between the two different operators. In the following, we simply drop the parameter c when there is no confusion.

3.2 Customized Sobolev space and approximation theory

With the help of Sturm-Liouville theory, one can define the following customized Sobolev space

$$H_c^s(B) := \{u \in L^2(B) : \sum_{\substack{l \in \mathbb{I}(m) \\ m, n \in \mathbb{N}}} \chi_{m,n}^s |\langle u, \psi_{m,n,\ell} \rangle|^2 < \infty\}$$

for any integer $s = 1, 2, \dots$, where $\langle u, \psi_{m,n,\ell} \rangle = \int_B u(x) \bar{\psi}_{m,n,\ell}(x) dx$ (here we have formally adopted the conjugate in the inner product but note that $\psi_{m,n,\ell}$ is real-valued). By interpolation theory [27], the above Sobolev space $H_c^s(B)$ is well defined for any real number $s \geq 0$.

Now for any function $u \in H_c^s(B)$, and its approximation

$$\pi_\epsilon u = \sum_{\substack{\chi_{m,n} < 1/\epsilon}} \langle u, \psi_{m,n,\ell} \rangle \psi_{m,n,\ell} \quad (10)$$

with a positive parameter $\epsilon > 0$, one can estimate the approximation error in $L^2(B)$.

Lemma 1. *Let $\epsilon > 0$ be a small positive parameter, and $\pi_\epsilon u$ be the approximation given by (10), then for any $u \in H_c^s(B)$, it holds that*

$$\|\pi_\epsilon u - u\|_{L^2(B)} < \epsilon^{s/2} \|u\|_{H_c^s(B)}. \quad (11)$$

Proof. For any $u \in H_c^s(B)$, it follows that

$$\begin{aligned} \|\pi_\epsilon u - u\|_{L^2(B)} &= \left\| \sum_{\substack{\chi_{m,n} > 1/\epsilon}} \langle u, \psi_{m,n,\ell} \rangle \psi_{m,n,\ell} \right\|_{L^2(B)} = \sum_{\substack{\chi_{m,n} > 1/\epsilon}} |\langle u, \psi_{m,n,\ell} \rangle|^2 \\ &\leq \epsilon^s \sum_{\substack{\chi_{m,n} > 1/\epsilon}} \chi_{m,n}^s |\langle u, \psi_{m,n,\ell} \rangle|^2 \leq \epsilon^s \|u\|_{H_c^s(B)}^2. \end{aligned}$$

This completes the proof. \square

The customized Sobolev space $H_c^s(B)$ can be related to the standard Sobolev space. In the inverse scattering problem, the unknown contrast may encounter non-smoothness, which motivates us to consider functions in $H^s(B)$ with $0 < s < 1$.

Lemma 2. If $u \in H^s(B)$ for any $0 < s < 1$, then $u \in H_c^s(B)$ and

$$\|u\|_{H_c^s(B)} \leq (1 + c^2)^{s/2} \|u\|_{H^s(B)}.$$

Proof. By the interpolation theory for Sobolev spaces [27], it is sufficient to prove the lemma for $s = 1$. For any smooth u , it follows from the definition of the Sturm-Liouville differential operator that

$$\begin{aligned} \|u\|_{H_c^1(B)}^2 &= \langle \mathcal{D}_c u, u \rangle = \int_B \left(-(1-r^2)\partial_r^2 u - \frac{2}{r}\partial_r u + 4r\partial_r u - \frac{1}{r^2}\Delta_{\mathbb{S}^2} u + c^2 r^2 u \right) \bar{u} dx \\ &= \int_0^\pi \int_0^{2\pi} \int_0^1 \left(-\sin \theta (r^2 - r^4) \partial_r^2 u - 2\sin \theta r \partial_r u + 4\sin \theta r^3 \partial_r u \right. \\ &\quad \left. - \sin \theta \left(\frac{1}{\sin \theta} \frac{\partial}{\partial \theta} \left(\sin \theta \frac{\partial u}{\partial \theta} \right) + \frac{1}{\sin^2 \theta} \frac{\partial^2 u}{\partial \phi^2} \right) + c^2 r^4 \sin \theta u \right) \bar{u} dr d\phi d\theta. \end{aligned}$$

To simplify the above formula, integration by parts yields that

$$\begin{aligned} &\int_0^\pi \int_0^{2\pi} \int_0^1 \left(-\sin \theta (r^2 - r^4) \partial_r^2 u - 2\sin \theta r \partial_r u + 4\sin \theta r^3 \partial_r u \right) \bar{u} dr d\phi d\theta \\ &= \int_0^\pi \int_0^{2\pi} \int_0^1 \sin \theta (r^2 - r^4) \partial_r u \partial_r \bar{u} dr d\phi d\theta, \end{aligned}$$

and

$$\begin{aligned} &\int_0^\pi \int_0^{2\pi} \int_0^1 \left(-\sin \theta \left(\frac{1}{\sin \theta} \frac{\partial}{\partial \theta} \left(\sin \theta \frac{\partial u}{\partial \theta} \right) + \frac{1}{\sin^2 \theta} \frac{\partial^2 u}{\partial \phi^2} \right) \bar{u} \right) dr d\phi d\theta \\ &= \int_0^\pi \int_0^{2\pi} \int_0^1 \left(\sin \theta \partial_\theta u \partial_\theta \bar{u} + \frac{1}{\sin \theta} \partial_\phi u \partial_\phi \bar{u} \right) dr d\phi d\theta. \end{aligned}$$

Use the above two identities one can conclude that

$$\begin{aligned} \|u\|_{H_c^1(B)}^2 &= \langle \mathcal{D}_c u, u \rangle = \int_B \left(-(1-r^2)\partial_r^2 u - \frac{2}{r}\partial_r u + 4r\partial_r u - \frac{1}{r^2}\Delta_{\mathbb{S}^2} u + c^2 r^2 u \right) \bar{u} dx \\ &= \int_0^\pi \int_0^{2\pi} \int_0^1 \left(\sin \theta (r^2 - r^4) \partial_r u \partial_r \bar{u} + \sin \theta \partial_\theta u \partial_\theta \bar{u} + \frac{1}{\sin \theta} \partial_\phi u \partial_\phi \bar{u} + c^2 r^4 \sin \theta u \bar{u} \right) dr d\phi d\theta. \end{aligned}$$

To connect with the standard Sobolev norm, one can proceed to estimate the above right hand side by

$$\begin{aligned} &\int_0^\pi \int_0^{2\pi} \int_0^1 \left(\sin \theta (r^2 - r^4) \partial_r u \partial_r \bar{u} + \sin \theta \partial_\theta u \partial_\theta \bar{u} + \frac{1}{\sin \theta} \partial_\phi u \partial_\phi \bar{u} + c^2 r^4 \sin \theta u \bar{u} \right) dr d\phi d\theta \\ &\leq \int_0^\pi \int_0^{2\pi} \int_0^1 \left(\sin \theta r^2 |\partial_r u|^2 + \sin \theta |\partial_\theta u|^2 + \frac{1}{\sin \theta} |\partial_\phi u|^2 + c^2 r^2 \sin \theta |u|^2 \right) dr d\phi d\theta \\ &= \|\nabla u\|_{L^2(B)}^2 + c^2 \|u\|_{L^2(B)}^2 \leq (c^2 + 1) \|u\|_{H^1(B)}^2, \end{aligned}$$

which allows to conclude that

$$\|u\|_{H_c^1(B)}^2 \leq (c^2 + 1) \|u\|_{H^1(B)}^2.$$

This completes the proof. \square

Finally, for any function $u \in H^s(B)$ with $0 < s < 1$, the following approximation error can be proved.

Theorem 1. Let $\epsilon > 0$ be a small positive parameter, and $\pi_\epsilon u$ be the approximation given by (10), then for any $u \in H^s(B)$ with $0 < s < 1$, it holds that

$$\|\pi_\epsilon u - u\|_{L^2(B)} < \epsilon^{s/2} (1 + c^2)^{s/2} \|u\|_{H^s(B)}. \quad (12)$$

Proof. From Lemma 1, it follows that $\|\pi_\epsilon u - u\|_{L^2(B)} < \epsilon^{s/2} \|u\|_{H_c^s(B)}$. Together with Lemma 2, one can complete the proof by $\|\pi_\epsilon u - u\|_{L^2(B)} < \epsilon^{s/2} \|u\|_{H_c^s(B)} \leq \epsilon^{s/2} (1 + c^2)^{s/2} \|u\|_{H^s(B)}$. \square

3.3 Low-rank approximation and a priori estimate

The data are inevitably corrupted by noise, this motivates us to consider noisy processed data u_b^δ such that

$$\|u_b^\delta - u_b\|_{L^2(B)} \leq \delta.$$

For example, the full far field data $u^\infty(\hat{x}; \hat{\theta}; k)$ will lead to such a perturbation u_b^δ .

Since the unknown contrast q is related to the processed data u_b via (7) and that the restricted Fourier integral operator has a low-rank structure, we are motivated to investigate a low-rank approximation of the noisy processed data given by

$$\pi_\epsilon u_b^\delta = \sum_{\chi_{m,n} \leq 1/\epsilon} \langle u_b^\delta, \psi_{m,n,\ell} \rangle \psi_{m,n,\ell},$$

which leads to the low-rank approximation of the unknown q given by

$$\pi_\epsilon q^\delta = \sum_{\chi_{m,n} \leq 1/\epsilon} \frac{\langle u_b^\delta, \psi_{m,n,\ell} \rangle}{\alpha_{m,n}} \psi_{m,n,\ell}. \quad (13)$$

In the following, we estimate the low-rank approximation error $q - \pi_\epsilon q^\delta$ under one of the following two assumptions: assumption (A) $q \in H_c^s(B)$ or assumption (B) $q \in \text{span}\{\psi_{m,n,\ell} : |\alpha_{m,n}| \geq \sigma\}$.

Theorem 2. *Assume that $q \in H_c^s(B)$. Let $\|u_b^\delta - u_b\|_{L^2(B)} \leq \delta$ for some $\delta > 0$ and the low-rank approximation of the unknown be given by (13) with some small regularization parameter $\epsilon > 0$. Then it holds that*

$$\|q - \pi_\epsilon q^\delta\|_{L^2(B)} \leq \epsilon^{s/2} (1 + c^2)^{s/2} \|q\|_{H^s(B)} + \frac{\delta}{\inf\{|\alpha_{m,n}| : \chi_{m,n} \leq 1/\epsilon\}}$$

Proof. Note that

$$\|q - \pi_\epsilon q^\delta\|_{L^2(B)} \leq \|q - \pi_\epsilon q\|_{L^2(B)} + \|\pi_\epsilon q - \pi_\epsilon q^\delta\|_{L^2(B)},$$

then we estimate each term on the right hand side as follows (where we will drop the $L^2(B)$ -norm when there is no confusion).

The first term on the right hand can be estimated by Theorem 1 where

$$\|q - \pi_\epsilon q\|_{L^2(B)}^2 \leq \epsilon^{s/2} (1 + c^2)^{s/2} \|q\|_{H^s(B)}.$$

The other term can be estimated by

$$\|\pi_\epsilon q - \pi_\epsilon q^\delta\| = \left\| \sum_{\chi_{m,n} \leq 1/\epsilon} \frac{\langle u_b^\delta - u_b, \psi_{m,n,\ell} \rangle}{\alpha_{m,n}} \psi_{m,n,\ell} \right\| \leq \frac{\|u_b^\delta - u_b\|_{L^2(B)}}{\inf\{|\alpha_{m,n}| : \chi_{m,n} \leq 1/\epsilon\}} \leq \frac{\delta}{\inf\{|\alpha_{m,n}| : \chi_{m,n} \leq 1/\epsilon\}}$$

The above three inequalities allows to prove the Theorem. This completes the proof. \square

Corollary 1. *Assume that $q \in \text{span}\{\psi_{m,n,\ell} : |\alpha_{m,n}| \geq \sigma\}$. Let $\|u_b^\delta - u_b\|_{L^2(B)} \leq \delta$ for some $\delta > 0$ and the low-rank approximation of the unknown be given by (13) with the regularization parameter $\epsilon = 1/\sup\{\chi_{m,n} : |\alpha_{m,n}| \geq \sigma\}$. Then it holds that*

$$\|q - \pi_\epsilon q^\delta\|_{L^2(B)} \leq \frac{\delta}{\sigma}.$$

Proof. Since by assumption that $q \in \text{span}\{\psi_{m,n,\ell} : |\alpha_{m,n}| \geq \sigma\}$, then with $\epsilon = 1/\sup\{\chi_{m,n} : |\alpha_{m,n}| \geq \sigma\}$, one can derive that $\|q - \pi_\epsilon q^\delta\|_{L^2(B)} = \|\pi_\epsilon q - \pi_\epsilon q^\delta\|_{L^2(B)}$. Following the proof in Theorem 2, one directly proves the Corollary. This completes the proof. \square

3.4 A versatile tool for regularization using H_c^s penalty term

The 3D PSWFs provide a versatile tool for regularization by penalizing the H_c^s -norm of solutions. Traditionally assuming the a priori knowledge that $q \in H^s$, one may consider the cost functional $\|\mathcal{F}^c q - u_b^\delta\|_{L^2}^2 + \eta \|q\|_{H^s}^2$ where the penalty term is $\eta \|q\|_{H^s}^2$ for some parameter $\eta > 0$. However, noting the relation between the standard Sobolev space H^s and the customized Sobolev space H_c^s in Section 3.2, we are motivated to consider the following cost functional

$$J_\eta(q) = \|\mathcal{F}^c q - u_b^\delta\|_{L^2}^2 + \eta \|q\|_{H_c^s}^2,$$

assuming the a priori knowledge that $q \in H_c^s$. One looks for q_η^δ that minimizes $J_\eta(q)$, i.e.,

$$q_\eta^\delta = \arg \min_q J_\eta(q).$$

Since the customized Sobolev space $H_c^s(B)$ is conveniently given by

$$H_c^s(B) = \{u \in L^2(B) : \sum_{m,n \in \mathbb{N}}^{l \in \mathbb{I}(m)} \chi_{m,n}^s |\langle u, \psi_{m,n,\ell} \rangle|^2 < \infty\},$$

one can reformulate the above minimization problem using the 3D PSWFs to derive the following regularized solution

$$q_\eta^\delta = \sum_{m,n \in \mathbb{N}}^{l \in \mathbb{I}(m)} \frac{\bar{\alpha}_{m,n}}{|\alpha_{m,n}|^2 + \eta \chi_{m,n}^s} \langle u_b^\delta, \psi_{m,n,\ell} \rangle \psi_{m,n,\ell}. \quad (14)$$

The difference between the low-rank regularized solution (13) and the above regularized solution (14) is due to the additional term $\eta \chi_{m,n}^s$, and this will be a straightforward modification since the Sturm-Liouville eigenvalues $\chi_{m,n}$ have been conveniently computed according to Section 4.1. Such convenient analytical and computational modification is again thanks to the dual property of 3D PSWFs. The idea of deriving a priori estimate for (14) is expected to be similar to the low-rank approximation and we omit it here. Numerical examples based on (14) will be provided.

3.5 A Localized imaging technique

The PSWFs are known to be double orthogonal [33]. This double orthogonality property will allow a localized imaging technique – imaging targeting objects inside a ball when there are possible complex objects around. This is motivated by, for example, fast imaging of a specific target despite the possible presence of surrounding objects (where one avoids parameterizing the surroundings or does not know the region to parameterize in). To be more precise, following [33] or [28] one can use the identity (8) to define the 3D PSWFs in \mathbb{R}^3 naturally via

$$\psi_{m,n,\ell}(x) = \frac{1}{\alpha_{m,n}} \int_B e^{icx \cdot y} \psi_{m,n,\ell}(y) dy, \quad x \in \mathbb{R}^3. \quad (15)$$

One can check via Fourier transform and the above (15) to verify the so-called double orthogonality property (see also [33])

$$\int_B \psi_{m,n,\ell} \bar{\psi}_{\tilde{m},\tilde{n},\tilde{\ell}} dx = \int_{\mathbb{R}^3} \psi_{m,n,\ell} \bar{\psi}_{\tilde{m},\tilde{n},\tilde{\ell}} dx = 0 \quad \text{when} \quad \{m, n, \ell\} \neq \{\tilde{m}, \tilde{n}, \tilde{\ell}\}, \quad (16)$$

$$1 = \int_B \psi_{m,n,\ell} \bar{\psi}_{\tilde{m},\tilde{n},\tilde{\ell}} dx = \frac{|\alpha_{m,n}|^2}{(2\pi/c)^3} \int_{\mathbb{R}^3} \psi_{m,n,\ell} \bar{\psi}_{\tilde{m},\tilde{n},\tilde{\ell}} dx \quad \text{when} \quad \{m, n, \ell\} = \{\tilde{m}, \tilde{n}, \tilde{\ell}\}. \quad (17)$$

The consequence of (17) is that the square energy (i.e., the square of the L^2 norm) of $\psi_{m,n,\ell}$ in B is $\frac{|\alpha_{m,n}|^2}{(2\pi/c)^3}$ of the square energy of $\psi_{m,n,\ell}$ in \mathbb{R}^3 , which implies that: for very small $|\alpha_{m,n}| \ll 1$, the principle energy of $\psi_{m,n,\ell}$ is in $\mathbb{R}^3 \setminus B$; for dominant prolate eigenvalues $|\alpha_{m,n}|$ close to $|\alpha_{0,0}|$, the principle energy of $\psi_{m,n,\ell}$ is in B . Intuitively speaking, the major information of unknowns in B is carried over by the 3D PSWFs with dominant prolate eigenvalues.

Having the above double orthogonality property, one can study the problem of imaging localized objects inside a ball when there are other objects around. The Born data are still given by (7) by changing the domain of integration to \mathbb{R}^3 so that

$$u_b(p; c) = \int_{\mathbb{R}^3} e^{icp \cdot \tilde{p}} q(\tilde{p}) d\tilde{p}. \quad (18)$$

Suppose that the unknown is given by $q = q_i + q_o$ where q_i is supported in B and q_o is supported in $\mathbb{R}^3 \setminus \overline{B}$. Denote by $\langle \cdot, \cdot \rangle_{\mathbb{R}^3}$ the inner product in $L^2(\mathbb{R}^3)$ and $\|\cdot\|_{\mathbb{R}^3}$ the corresponding $L^2(\mathbb{R}^3)$ norm. We add subscript B to indicate the inner product and norm are for the domain B . Equation (18) leads to

$$\begin{aligned} \langle u_b, \psi_{m,n,\ell} \rangle_B &= \int_B \int_{\mathbb{R}^3} e^{icx \cdot y} (q_i(y) + q_o(y)) \psi_{m,n,\ell}(x) dy dx \\ &= \int_B \int_B e^{icx \cdot y} q_i(y) dy \psi_{m,n,\ell}(x) dx + \int_B \int_{\mathbb{R}^3 \setminus \overline{B}} e^{icx \cdot y} q_o(y) dy \psi_{m,n,\ell}(x) dx \\ &= \int_B \alpha_{m,n} \psi_{m,n,\ell}(y) q_i(y) dy + \int_{\mathbb{R}^3 \setminus \overline{B}} \alpha_{m,n} \psi_{m,n,\ell}(y) q_o(y) dy \end{aligned}$$

and one can arrive at

$$\frac{1}{\alpha_{m,n}} \langle u_b, \psi_{m,n,\ell} \rangle_B = \langle q_i, \psi_{m,n,\ell} \rangle_{\mathbb{R}^3} + \langle q_o, \psi_{m,n,\ell} \rangle_{\mathbb{R}^3}, \quad (19)$$

noting that q_i is supported in B and q_o is supported in $\mathbb{R}^3 \setminus \overline{B}$. When the principal energy of $\psi_{m,n,\ell}$ is in the unit ball B , one can expect that the last quantity $\langle q_o, \psi_{m,n,\ell} \rangle_{\mathbb{R}^3}$ in (19) is small so that $\frac{1}{\alpha_{m,n}} \langle u_b, \psi_{m,n,\ell} \rangle_B$ gives an approximation of $\langle q_i, \psi_{m,n,\ell} \rangle_{\mathbb{R}^3} = \langle q_i, \psi_{m,n,\ell} \rangle_B$. This leads to the approximation

$$q_i^\sigma(x) = \sum_{|\alpha_{m,n}| > \sigma} \frac{1}{\alpha_{m,n}} \langle u_b, \psi_{m,n,\ell} \rangle_B \psi_{m,n,\ell}(x)$$

where σ is chosen close to the dominant prolate eigenvalues. We will demonstrate this property in the numerical study with $\sigma = 0.9|\alpha_{0,0}|$.

4 Computational framework

In this section we develop the computational framework for computing the low-rank approximation of the inverse solution. The computation of the 3D PSWFs will be based on the dual property where the 3D PSWFs are both eigenvalues of the restricted Fourier integral operator and the Sturm-Liouville differential operator. The low-rank approximation will be derived by processing the far field data and projecting the processed data onto a low-rank space.

4.1 Computation of 3D PSWFs and prolate eigenvalues

The 3D PSWF $\psi_{m,n,\ell}(x; c)$ can be represented by the following series of ball polynomial (cf. [33], [37])

$$\psi_{m,n,\ell}(x; c) = \sum_{j=0}^{\infty} \beta_j^{m,n}(c) P_{m,j,\ell}(x), \quad x \in B, \quad (20)$$

where the ball polynomial is defined by $P_{m,j,\ell}(x) = r^m P_j^{(m)}(2r^2 - 1) Y_{m,\ell}(\hat{x})$. Here $Y_{m,\ell}(\hat{x})$ represents the (real-valued) spherical harmonics and $P_n^{(m)}$ represents the normalized Jacobi polynomial, whose definitions are given below.

Spherical harmonics. The complex spherical harmonics can be found in [10], which can be used to derive the following real-valued spherical harmonic $Y_{m,\ell}(\hat{x})$ given by

$$Y_{m,\ell}(\hat{x}) = \begin{cases} \sqrt{\frac{2m+1}{4\pi}} P_m(\cos \theta), & \ell = 0 \\ \sqrt{\frac{2m+1}{2\pi} \frac{(m-|\ell|)!}{(m+|\ell|)!}} P_m^{\ell}(\cos \theta) \cos(\ell\phi), & \ell = 1, 2, \dots, m \\ \sqrt{\frac{2m+1}{2\pi} \frac{(m-|\ell|)!}{(m+|\ell|)!}} P_m^{|\ell|}(\cos \theta) \sin(\ell\phi), & \ell = -1, -2, \dots, -m \end{cases}, \quad (21)$$

where P_m^ℓ is the associated Legendre function given by

$$P_m^\ell(r) = (1 - r^2)^{\ell/2} \frac{d^\ell}{dx^\ell} P_m(x), \quad -1 < r < 1, \quad 0 \leq \ell \leq m$$

with P_m being the Legendre polynomial of order m , c.f., [1, 10]. Such spherical harmonic $Y_{m,\ell}(\hat{x})$ is the eigenfunction of the Laplace-Beltrami operator, i.e.,

$$\Delta_{\mathbb{S}^2} Y_{m,\ell}(\hat{x}) = -m(m+1)Y_{m,\ell}(\hat{x}),$$

and satisfies the orthonormal condition

$$\langle Y_{m,\ell}, Y_{\tilde{m},\tilde{\ell}} \rangle_{L^2(\mathbb{S}^2)} = \delta_{m,\tilde{m}} \delta_{\ell,\tilde{\ell}}.$$

More details about spherical harmonics can be found in [1, 10].

Jacobi polynomials. The normalized Jacobi polynomials $\{P_n^{(m)}(\eta)\}_{\eta \in (-1,1)}^{n \in \mathbb{N}}$ mentioned above are eigenfunctions of the following Sturm-Liouville problem,

$$-\frac{1}{w_{m+1/2}(\eta)} \partial_\eta \left((1-\eta) w_{m+3/2}(\eta) \partial_\eta P_n^{(m)}(\eta) \right) = n(n+m+3/2) P_n^{(m)}(\eta), \quad -1 < \eta < 1 \quad (22)$$

where $w_{m+1/2}(\eta) = (1+\eta)^{m+1/2}$, and they satisfy the orthogonality condition and are normalized by

$$\int_{-1}^1 w_{m+1/2}(\eta) P_n^{(m)}(\eta) P_{\tilde{n}}^{(m)}(\eta) d\eta = 2^{m+5/2} \delta_{n\tilde{n}}, \quad \forall n, \tilde{n} \in \mathbb{N}. \quad (23)$$

The normalized Jacobi polynomials $\{P_n^{(m)}(\eta)\}_{\eta \in (-1,1)}$ satisfy the following three-term recurrence relation

$$P_{n+1}^{(m)}(\eta) = \frac{(x - b_n) P_n^{(m)}(\eta) - a_{n-1} P_{n-1}^{(m)}(\eta)}{a_n}, \quad n \geq 1$$

with the first two terms given by

$$P_0^{(m)}(\eta) = \frac{1}{h_0}, \quad P_1^{(m)}(\eta) = \frac{(m+5/2)\eta - m - 1/2}{2h_1},$$

here a_n , b_n , and h_n are given by

$$\begin{cases} a_n = \frac{2(n+1)(n+m+3/2)}{(2n+m+5/2)\sqrt{(2n+m+3/2)(2n+m+7/2)}} \\ b_n = \frac{(m+1/2)^2}{(2n+m+1/2)(2n+m+5/2)} \\ h_n = \frac{1}{\sqrt{2(2n+m+3/2)}} \end{cases}, \quad n \in \mathbb{N}. \quad (24)$$

For a more comprehensive introduction to special polynomials, we refer to [1]. From the definition of the normalized Jacobi polynomial and the spherical harmonics, it is seen that $\|P_{m,j,l}\|_{L^2(B)} = 1$.

Computation of 3D PSWFs system. To compute $\{\beta_j^{m,n}\}_{j \in \mathbb{N}}$, we plug the expansion (20) into (9) and we can derive that the coefficients satisfy

$$\left(\gamma_{m+2j} + \frac{(1+b_j)c^2}{2} - \chi_{m,n}(c) \right) \beta_j^{m,n} + \frac{a_{j-1}c^2}{2} \beta_{j-1}^{m,n} + \frac{a_jc^2}{2} \beta_{j+1}^{m,n} = 0, \quad j \geq 0 \quad (25)$$

where $\gamma_{m+2j} = (m+2j)(m+2j+3)$. Here $\chi_{m,n}(c)$ is the Sturm-Liouville eigenvalue. This is an infinite linear system. In practice, one can start with the approximation

$$\tilde{\psi}_{m,n,l}(x; c) = \sum_{j=0}^K \tilde{\beta}_j^{m,n} P_{m,j,l}(x), \quad 2n+m \leq N, \quad (26)$$

so that the coefficients $\{\tilde{\beta}_j^{m,n}\}$ can be solved from the following tridiagonal linear system

$$A\tilde{\beta}^{m,n} = \tilde{\chi}_{m,n}\tilde{\beta}^{m,n} \quad (27)$$

with eigenvalues $\tilde{\chi}_{m,n}$, where $\tilde{\beta}^{m,n} = (\tilde{\beta}_0^{m,n}, \tilde{\beta}_1^{m,n}, \dots, \tilde{\beta}_K^{m,n})^T$, A is a $(K+1) \times (K+1)$ symmetric tridiagonal matrix whose nonzero entries are given by

$$A_{j,j} = \gamma_{m+2j} + \frac{(1+b_j)c^2}{2} \quad \text{and} \quad A_{j,j+1} = A_{j+1,j} = \frac{a_j c^2}{2}, \quad j \geq 0.$$

Since the 3D PSWFs are normalized to have unit $L^2(B)$ -norm, the coefficient vector $\tilde{\beta}^{m,n}$ are set to satisfy

$$\|\tilde{\beta}^{m,n}\|_2 = \left(\sum_{j=0}^K |\tilde{\beta}_j^{m,n}|^2 \right)^{1/2} = 1.$$

The eigenvalues are sorted according to

$$\tilde{\chi}_{m,j} < \tilde{\chi}_{m,i}, \quad j < i.$$

In practice, the number K of truncated terms in (26) can be chosen as $K = \left\lceil \frac{M-m}{2} \right\rceil$, c.f., [37].

Finally to evaluate the prolate eigenvalues $\{\alpha_{m,n}\}_{m,n \in \mathbb{N}}$, the following formula was given in [37]

$$\tilde{\alpha}_{m,n}(c) = \frac{\pi^{3/2}(ic)^m}{2^{m-\frac{1}{2}} \sqrt{\Gamma(m+3/2)\Gamma(m+5/2)}} \frac{\tilde{\beta}_0^{m,n}}{\tilde{\varphi}_{m,n}(-1; c)} \quad (28)$$

where $\tilde{\varphi}_{m,n}(-1; c) = \sum_{j=0}^K \tilde{\beta}_j^{m,n} P_j^{(m)}(-1)$ and note that i is the imaginary unit here. This formula with $N = K = 150$ is sufficient for our inverse problem.

We summarize the following algorithm for the evaluation of PSWFs and prolate eigenvalues.

Algorithm 1 Evaluation of 3D PSWF and prolate eigenvalue

Input: Parameter c , index of 3D PSWF (m, n, l) and $x \in \mathbb{R}^2$.

Output: $\psi_{m,n,l}(x; c)$ and prolate eigenvalue $\alpha_{m,n}(c)$.

- 1: Compute the tridiagonal linear system (27) (and sort the eigenvalues from small to large) to obtain the eigenvector $\tilde{\beta}^{m,n}$ and the eigenvalue $\tilde{\chi}_{m,n}(c)$ corresponding to the given (m, n) . Here $\tilde{\beta}^{m,n} = (\tilde{\beta}_0^{m,n}, \tilde{\beta}_1^{m,n}, \dots, \tilde{\beta}_K^{m,n})^T$.
- 2: Evaluate $(P_{m,0}(2\|x\|^2 - 1), P_{m,1}(2\|x\|^2 - 1), \dots, P_{m,K}(2\|x\|^2 - 1))^T$ at $x \in \mathbb{R}^3$ by the recurrence (24) and the spherical harmonics $Y_{m,l}(\hat{x})$ at \hat{x} by (21).
- 3: Compute the approximation of 3D PSWFs by $\tilde{\psi}_{m,n,l}(x; c) = \|x\|^m Y_{m,l}(\hat{x}) \sum_{j=0}^K \tilde{\beta}_j^{m,n} P_j^{(m)}(2\|x\|^2 - 1)$.
- 4: Evaluate the prolate eigenvalue $\tilde{\alpha}_{m,n}(c)$ according to (28).

4.2 Computation of inverse solution in the low-rank space

To evaluate the low-rank approximation (13), one needs to evaluate the projection $\langle u_b^\delta, \psi_{m,n,\ell} \rangle$. Here we follow the Gaussian product quadrature where the quadrature points are given by

$$\mathbb{P} := \left\{ \sqrt{(1+t_i)/2} \begin{pmatrix} \sin \theta_s \cos \phi_j \\ \sin \theta_s \sin \phi_j \\ \cos \theta_s \end{pmatrix} : \begin{array}{l} i = 0, 1, \dots, T-1 \\ s = 0, 1, \dots, M_\theta - 1 \\ j = 0, 1, \dots, M_\phi - 1 \end{array} \right\} = \{p_n : n = 1, 2, \dots, TM_\theta M_\phi\},$$

here each p_n is uniquely associated with an index (i, s, j) , and $\{t_i, \theta_s, \phi_j\}_{i=0, s=0, j=0}^{T-1, M_\theta-1, M_\phi-1}$ are chosen according to

$$\{t_i, \omega_{t_i}\}_{i=0}^{T-1}, \{\cos \theta_s, \omega_{\theta_s}\}_{s=0}^{M_\theta-1} : \quad \text{Gauss-Legendre quadrature nodes and weights}, \quad (29)$$

$$\left\{ \phi_j = \frac{2j\pi}{M_\phi}, \omega_{\phi_j} = \frac{2\pi}{M_\phi} \right\}_{j=0}^{M_\phi-1} : \quad \text{trapezoidal quadrature nodes and weights}. \quad (30)$$

With such a quadrature, the projection is evaluated by

$$\langle u_b^\delta, \psi_{m,n,\ell} \rangle \approx \frac{\pi}{2\sqrt{2}M_\phi} \sum_{i=0}^{T-1} \sum_{j=0}^{M_\phi-1} \sum_{s=0}^{M_\theta-1} u_b^\delta(p_n; c) \psi_{m,n,l}(t_i, \phi_j, \theta_s) (1+t_i)^{1/2} w_{t_i} w_{\theta_s},$$

where again p_n is uniquely associated with an index (i, s, j) .

The data $\{u_b^\delta(p_n; c) : p_n \in \mathbb{P}, n = 1, 2, \dots, TM_\phi M_\theta\}$ will be determined by the full or Born noisy far field data via the relation (6) in the continuous case. In practice when the numbers of observation and incident directions are finite, we look for approximate or mock-quadrature nodes $\{\tilde{p}_n\}_{n=1}^{T \times M_\phi \times M_\theta}$ given by

$$\tilde{p}_n = \frac{\hat{\theta}_{\ell^*} - \hat{x}_{j^*}}{2}, \text{ where } (\ell^*, j^*) = \underset{1 \leq j \leq N_1, 1 \leq \ell \leq N_2}{\operatorname{argmin}} \left\| p_n - \frac{\hat{\theta}_\ell - \hat{x}_j}{2} \right\|_2, \quad (31)$$

and we approximate the *processed data* set $\{u_b^\delta(p_n; c) : p_n \in P, n = 1, 2, \dots, TM_\phi M_\theta\}$ by

$$\{u_b^\delta(\tilde{p}_n; c) = \frac{4\pi}{k^2} u^{\infty, \delta}(\hat{x}_{j^*}; \hat{\theta}_{\ell^*}; k) : \tilde{p}_n = \frac{\hat{\theta}_{\ell^*} - \hat{x}_{j^*}}{2}, 1 \leq n \leq TM_\phi M_\theta\}. \quad (32)$$

If the far field data set is of large scale such as when $N_1 \times N_2 \geq T \times M_\phi \times M_\theta$, one can process the far field data set of dimension $N_1 \times N_2$ to get a smaller processed data set through the relation (31)–(32); Otherwise if the far field data are limited, one can extend the data set through nearest interpolation for simplicity following by applying the relation (31)–(32). It is worth mentioning other options to use specific quadrature such as [14], which is a possible future direction.

As a result, the numerical low-rank approximation is given by

$$q^{\sigma, \delta} = \sum_{|\alpha_{m,n}| > \sigma} \frac{1}{\alpha_{m,n}} \left(\frac{\pi}{2\sqrt{2}M_\phi} \sum_{i=0}^{T-1} \sum_{j=0}^{M_\phi-1} \sum_{s=0}^{M_\theta-1} u_b^\delta(\tilde{p}_n; c) \psi_{m,n,l}(t_i, \phi_j, \theta_s) (1+t_i)^{1/2} w_{t_i} w_{\theta_s} \right) \psi_{m,n,l},$$

where each \tilde{p}_n is uniquely associated with an index (i, s, j) . We summarize the low-rank computational framework, from data entry to output, by Algorithm 2.

Algorithm 2 Low rank solution for inverse scattering problem

Input: Wave number k , noisy full far field data $\{u^{\infty, \delta}(\hat{x}_j; \hat{\theta}_\ell; k) : j = 1, 2, \dots, N_1, \ell = 1, 2, \dots, N_2\}$, or noisy Born far field pattern data $\{u_b^{\infty, \delta}(\hat{x}_j; \hat{\theta}_\ell; k) : j = 1, 2, \dots, N_1, \ell = 1, 2, \dots, N_2\}$.

Output: The low-rank approximation $q^{\sigma, \delta}$ of the unknown.

- 1: Set $c = 2k$ and spectral cutoff regularization parameter σ . Set $\mathcal{J}_\sigma = \{(m, n, \ell) : |\alpha_{m,n}| > \sigma\}$.
- 2: (Precomputing) Apply Algorithm 1 to evaluate the 3D PSWFs at quadrature nodes, i.e., $\{\psi_{m,n,l}(p_n; c) : (m, n, l) \in \mathcal{J}_\sigma, 1 \leq n \leq TM_\phi M_\theta\}$ and the prolate eigenvalues $\{\alpha_{m,n}(c) : (m, n, 0) \in \mathcal{J}_\sigma\}$.
- 3: Apply (31)–(32) to obtain the processed data $\{u_b^\delta(\tilde{p}_n; c)\}_{n=1}^{TM_\phi M_\theta}$.
- 4: Calculate the projection of processed data on the low-rank space via (29)–(30) and

$$u_{m,n,l}^{\sigma, \delta} \approx \frac{\pi}{2\sqrt{2}M_\phi} \sum_{s=0}^{M_\theta-1} \sum_{i=0}^{T-1} \sum_{j=0}^{M_\phi-1} u_b^\delta(\tilde{p}_n; c) \psi_{m,n,l}(t_i, \phi_j, \theta_s) (1+t_i)^{1/2} w_{t_i} w_{\theta_s}, \quad (m, n, l) \in \mathcal{J}_\sigma.$$

- 5: Evaluate $q_{m,n,l}^{\sigma, \delta} = u_{m,n,l}^{\sigma, \delta} / \alpha_{m,n}$ to obtain the low-rank approximation

$$q^{\sigma, \delta}(x; c) = \sum_{(m, n, l) \in \mathcal{J}_\sigma} q_{m,n,l}^{\sigma, \delta} \psi_{m,n,l}(x; c).$$

5 Numerical experiments

In this section, we provide various numerical examples using both the Born far field data (5) and the full far field data (3). We will illustrate the potential of the proposed method via studies of imaging resolution, robustness, comparison with an iterative method, regularization using customized penalty, and localized imaging.

5.1 Data generation

5.1.1 Born processed data

Let us start with the simple case of Born processed data. One can generate the Born processed data by directly calculating the restricted Fourier integral (7) with the following given contrasts q .

- Constant in a ball $q(x) = 1_{x \in \Omega}(x)$, $\Omega = \{x \in \mathbb{R}^3 : \|x\|_2 < a\}$, $a < 1$. This leads to

$$u_b(x; c) = \left(\frac{2a\pi}{c\|x\|} \right)^{3/2} J_{3/2}(ac\|x\|),$$

where $J_{3/2}$ is Bessel function of the first kind of order $\nu = 3/2$, see [1]. In the following numerical experiments, we set $a = 0.5$.

- Constant in a cube $q(x) = 1_{x \in \Omega}(x)$, $\Omega = \{x \in \mathbb{R}^3 : a_j \leq x_j \leq b_j, j = 1, 2, 3\} \subset B(0, 1)$. This leads to

$$u_b(x; c) = \prod_{j=1}^3 \frac{1}{icx_j} (e^{icx_j \cdot b_j} - e^{icx_j \cdot a_j}).$$

We test $a_j = -1/2$, $b_j = 1/2$ in our numerical experiment.

Furthermore, we will test constant contrast supported in three nearby cubes: $q = 1_{\cup_{j=1}^3 \Omega_j}$ given by

$$\begin{cases} \Omega_1 := \{(x_1, x_2, x_3) \in \mathbb{R}^3 : |x_1| \leq 0.3, -0.5 < x_2 < -0.025, 0.1 < x_3 < 0.5\}, \\ \Omega_2 := \{(x_1, x_2, x_3) \in \mathbb{R}^3 : |x_1| \leq 0.3, 0.025 < x_2 < 0.5, 0.1 < x_3 < 0.5\}, \\ \Omega_3 := \{(x_1, x_2, x_3) \in \mathbb{R}^3 : |x_1| \leq 0.3, -0.235 < x_2 < 0.235, -0.5 < x_3 < 0.025\} \end{cases}. \quad (33)$$

- Oscillatory contrast $q(x_1, x_2, x_3) = \sin(m\pi x_1) \cdot 1_{\Omega}(x)$, $\Omega = \{x \in \mathbb{R}^3 : |x_j| < 1/2, j = 1, 2, 3\}$, $m \in \mathbb{Z}$. This leads to

$$u_b(x; c) = -8i \left(\frac{\sin(cx_1 + m\pi)/2}{cx_1 + m\pi} - \frac{\sin(cx_1 - m\pi)/2}{cx_1 - m\pi} \right) \prod_{j=2}^3 \frac{\sin(cx_j/2)}{cx_j}.$$

In the following numerical experiments, we test $m = 8$.

To test robustness of the proposed method, randomly distributed noise are added to the processed Born data u_b to generate the noisy data

$$u_b^{\tilde{\delta}}(p_n; c) = u_b(p_n; c)(1 + \delta \xi_n), \quad p_n \in \mathbb{P}, \quad (34)$$

where the set \mathbb{P} is given in Section 4.2, $\xi_n \in [-1, 1]$ is a uniformly distributed random number and $\delta \in [0, 1]$ is referred to as the noise level. It follows that $\|u_b^{\tilde{\delta}} - u_b\| \leq \delta \|u_b\| = \tilde{\delta}$. In the following, the regularization parameter is chosen as $\sigma = \delta \alpha_{0,0}(c)$ when $\delta > 0$ and $\sigma = 0.1 |\alpha_{0,0}(c)|$ when $\delta = 0$.

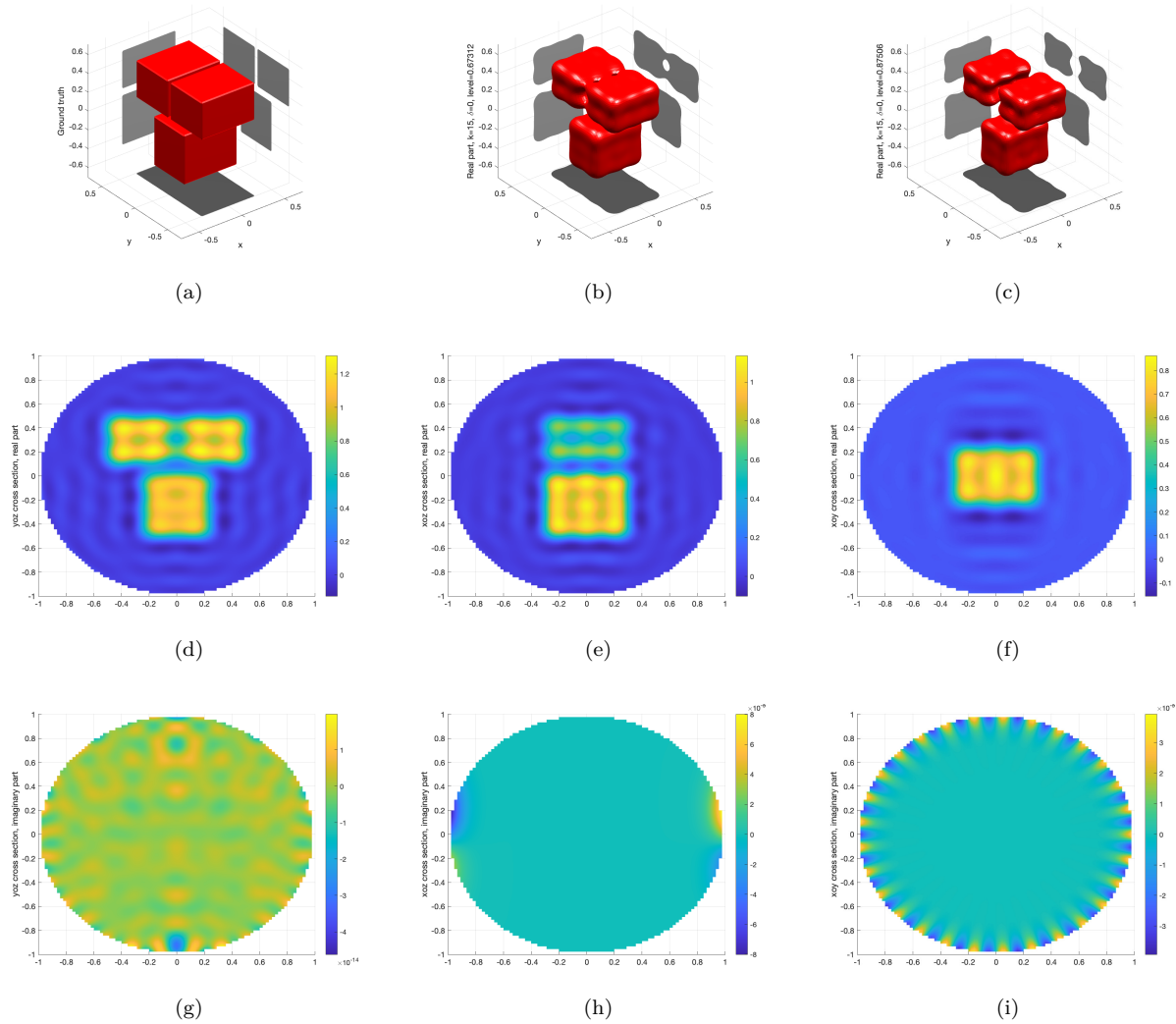


Figure 1: Reconstruction of three cubes with noiseless processed data, $k = 15$, $T = 23$, $M_\theta = 31$, $M_\phi = 61$. The first row (a) ground truth, (b) (c) isosurfaces of reconstruction (real part) with level value $0.5M$, $0.65M$, where $M = \max q^{\sigma, \delta}$; the second (resp. third) row, cross section view of the real (resp. imaginary) part.

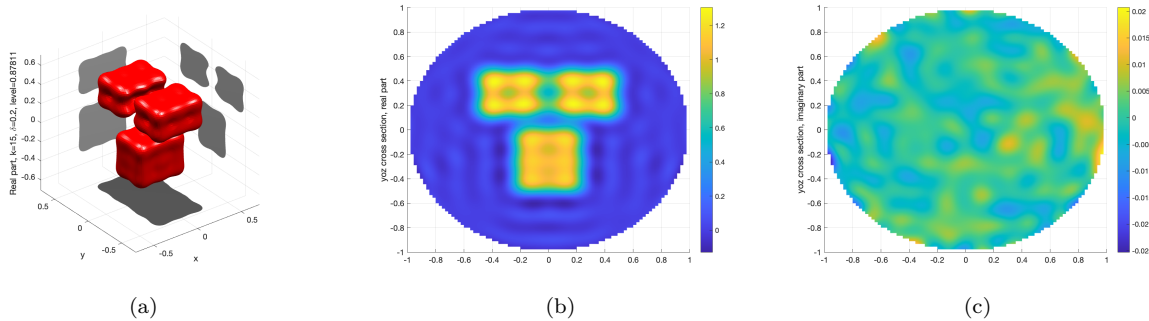


Figure 2: Reconstruction of three cubes with noisy processed data, $\delta = 0.2$ and all other parameters are the same as Figure 1.

5.1.2 Far field data

Born far field data. The discrete Born far field data are given at incident directions $\{\hat{\theta}_\ell\}_{\ell=1}^{N_2}$ and observation direction $\{\hat{x}_j\}_{j=1}^{N_1}$; both $\{\hat{\theta}_\ell\}_{\ell=1}^{N_2}$ and $\{\hat{x}_j\}_{j=1}^{N_1}$ follow the Fibonacci lattice on the sphere \mathbb{S}^2 , which was studied in geosciences [12]. Having the analytic formula in (5.1.1), Born far field data can be generated by,

$$u_b^\infty(\hat{x}_j; \hat{\theta}_\ell; k) = \frac{k^2}{4\pi} u_b\left(\frac{\hat{\theta}_\ell - \hat{x}_j}{2}; 2k\right), \quad 1 \leq j \leq N_1, \quad 1 \leq \ell \leq N_2. \quad (35)$$

Full far field data. To test the performance of the proposed method with the fully nonlinear model, we use the Matlab toolbox IPscatt [5] to generate the full far field data

$$\{u^\infty(\hat{x}_j; \hat{\theta}_\ell; k) : 1 \leq j \leq N_1, 1 \leq \ell \leq N_2\}.$$

To characterize the error between Born model (4) and the full model (2), we follow [5] to introduce the relative modeling error by $\text{rel}(k) = \frac{\|U - U_b\|_2}{\|U\|_2}$, where $U = (u_j^s(x_n))_{n=1}^{NN_2}$, $U_b = (u_{b,j}^s(x_n))_{N_2 \times N}$; each $u_j^s(x_n)$ and $u_{b,j}^s(x_n)$ with $j \in \{1, 2, \dots, N_2\}$ is the radiating solution of full model and the Born model due to the j -th incident wave $e^{ik\hat{\theta}_j \cdot x}$, respectively; here $\{x_n\}_{n=1}^N$ is a set of discretization points in the domain of interest $[-\frac{\sqrt{2}}{2}, \frac{\sqrt{2}}{2}]^3$, and N is set to 91³ in the numerical experiments.

Processed noisy data. After generating the far field data, the processed data are further generated by $u_b(\tilde{p}_n; c) = \frac{4\pi}{k^2} u_b^\infty(\hat{x}_{j^*}; \hat{\theta}_{\ell^*}; k)$ according to (31)–(32), where we recall that $\tilde{p}_n = \frac{\hat{\theta}_{\ell^*} - \hat{x}_{j^*}}{2}$ is the approximate quadrature node. Noisy data u_b^δ are again generated according to (34); in the case of full far field data, one simply repeats the above procedure with $u_b(\cdot; c)$ being replaced by $u(\cdot; c)$. The regularization parameter is set to $\epsilon = 0.9|\alpha_{0,0}|$ to maintain robustness, as we assume no prior information of modeling error.

5.2 Numerical results

5.2.1 Reconstruction using Born processed data

We first test the proposed method by reconstructing three cubes using directly the Born processed data given in Section 5.1.1, with noise level $\delta = 0$ (Figure 1) and $\delta = 0.2$ (Figure 2), respectively. The ground truth of the three cubes is given in Figure 1 (a), the reconstructions are plotted using both isosurface and the cross-section views. The proposed method yields good reconstructions in this case when the smallest distance between cubes is 0.05 which is smaller than half wavelength $\pi/k \approx 0.21$. The proposed method also performs well using noisy processed data, see Figure 2. This demonstrates the potential of the proposed method.

5.2.2 Reconstruction using Born far field data

The previous processed data are generated directly by analytic formula. To illustrate the effect of the data processing using (31)–(32), We next conduct experiments using the Born far field data as described in (35) for three different cases. The number of incident and observation directions are $N_1 = N_2 = 201$, which are distributed according to the Fibonacci lattice on the sphere. Additionally, noises are added to the data through (34). In Figure 3, the left column is for a ball, the middle column is for a cube, and the right column is for an oscillating contrast, respectively. The top row shows the ground truth, the middle row shows the isosurface view of the reconstruction, and the bottom row shows the cross section view of the reconstruction, respectively.

5.2.3 Reconstruction using full far field data (nonlinear model)

After successfully testing the Born data, we shift our focus to the full far field data where the modeling error is not overly large. In particular the largest amplitudes of the contrast “cross3D” and “three cubes” are 0.03 and 0.02, respectively. To shed light on the changes of resolution with respect to the wave number, we test $k \in \{10, 15, 20\}$. As is observed in Figure 4 and Figure 5, the resolution improves as the wave number k increases.

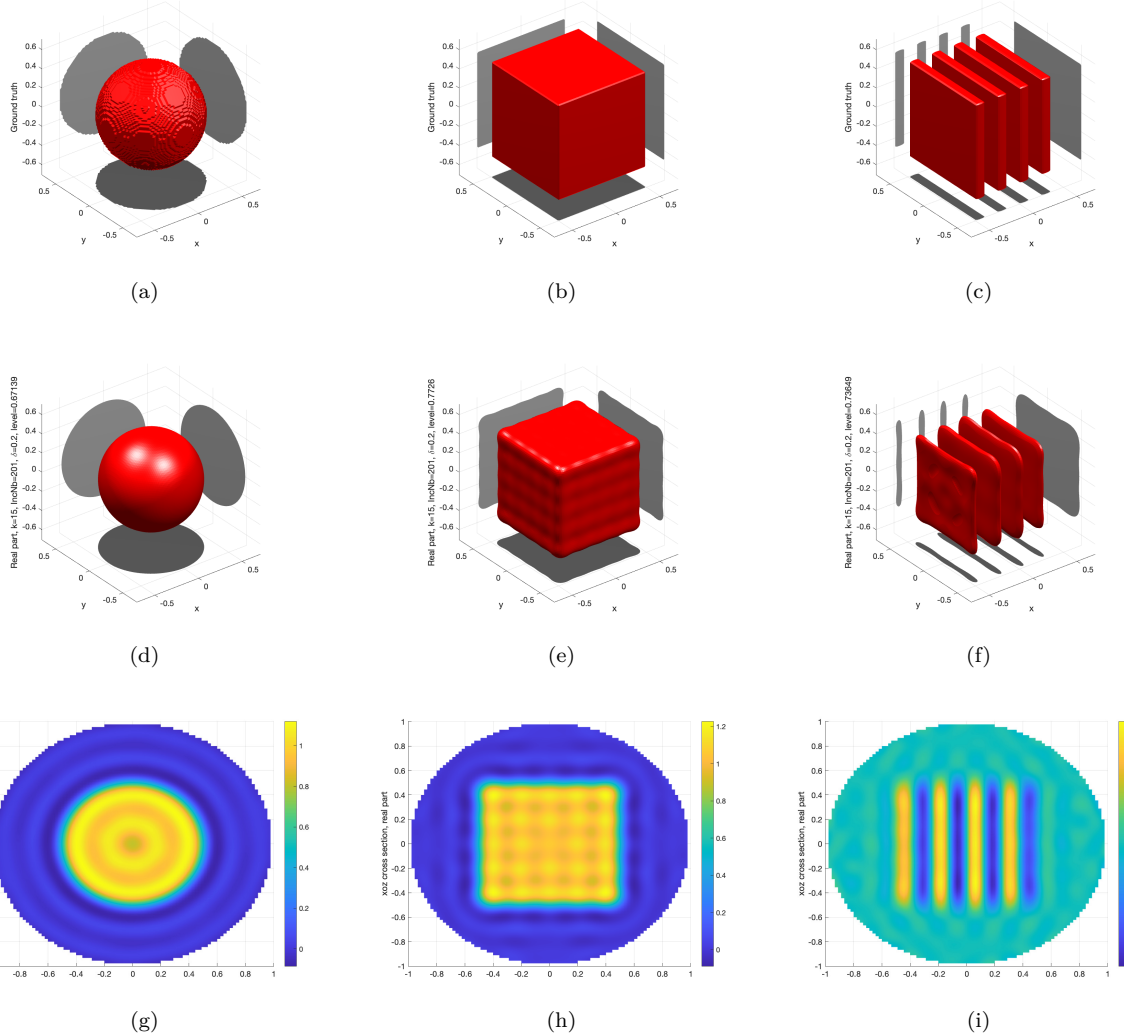


Figure 3: Reconstruction of three contrasts with Born far field data with $k = 15$, $\delta = 0.2$, and $N_1 = N_2 = 201$. The first row: isosurface view of ground truth; the second row: isosurface of reconstruction; the third row: cross section view of the reconstruction of a ball, a cube and the oscillatory contrast, respectively.

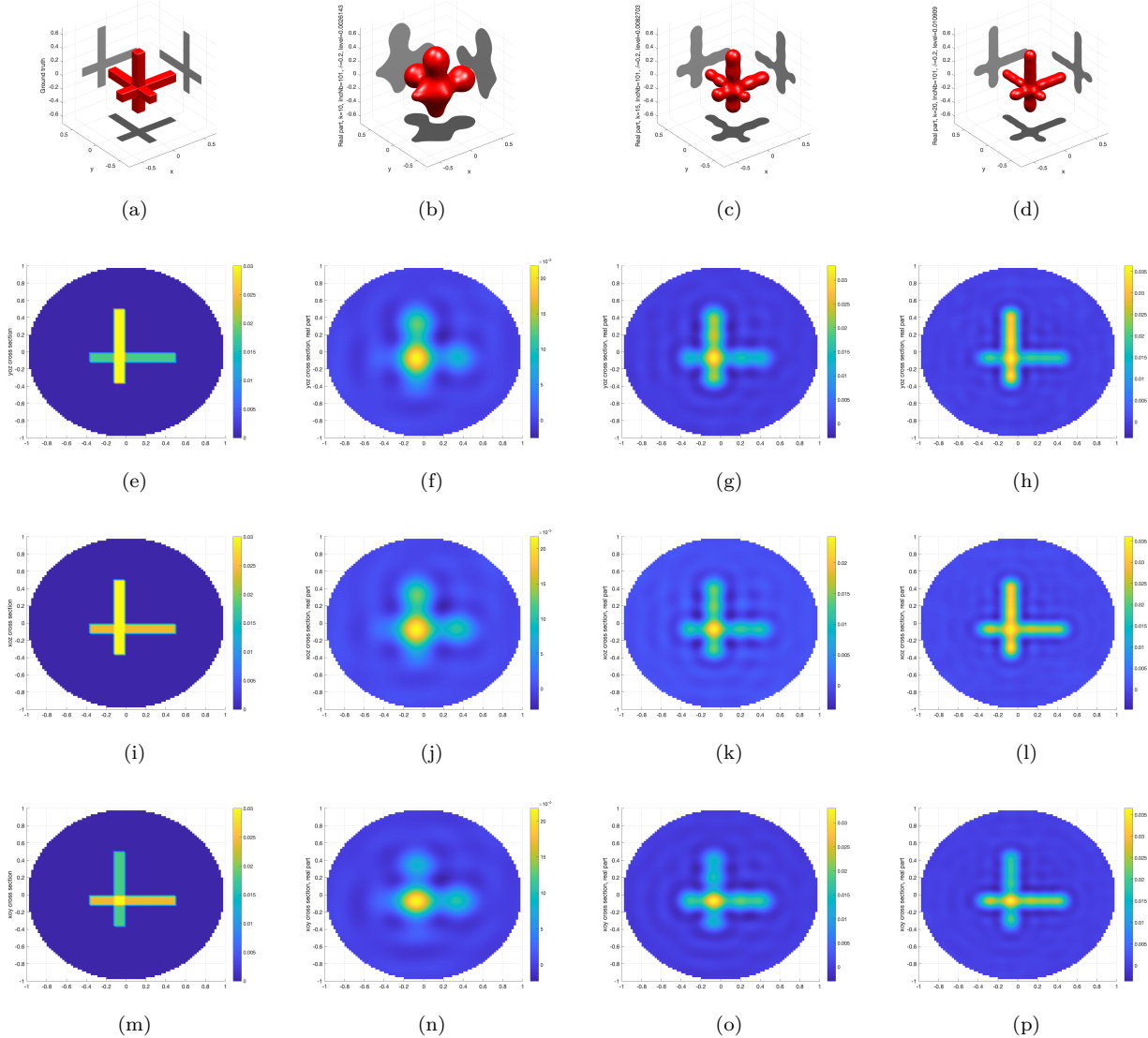


Figure 4: Reconstruction of “cross3D” using full far field data with observation and incident direction pairs $N_1 \times N_2 = 101 \times 101$ and noise level $\delta = 0.2$. The modeling error is $\text{rel}(k) = 1.82\%, 3.28\%, 4.75\%$, respectively for $k = 10, 15, 20$. The first column: ground truth. The second, third, and fourth columns: reconstructions using $k = 10, 15, 20$, respectively. From the top to the bottom row: isosurface and the cross section views. The width of each bar is $1/8$, and the length is $7/8$. The protruding part on the shorter side is $1/4$ in length.

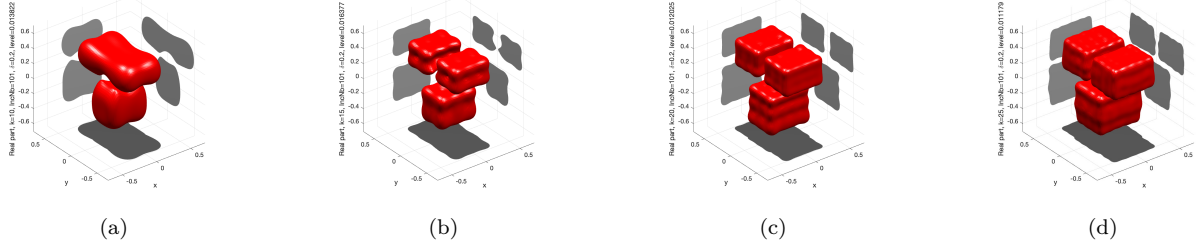


Figure 5: Reconstruction of three cubes using full far field data with observation and incident direction pairs $N_1 \times N_2 = 101 \times 101$ and noise level $\delta = 0.2$. The modeling error is $\text{rel}(k) = 1.82\%, 3.28\%, 9.15\%, 11.13\%$ for $k = 10, 15, 20, 25$, respectively.

5.2.4 Comparison with an iterative method

Iterative methods typically construct a minimization functional with regularization terms and use optimization to find the minimum. The regularization terms need certain prior information about the contrast. The Toolbox IPscatt [5] offers a built-in iterative method, based on the assumption that the contrast is sparse and has sharp edges. In iterative methods, technical difficulties may arise due to choice of regularization parameter, computational cost, as well as local minima. The proposed method based on the low-rank structure is a direct reconstruction method, which does not require any prior information about the contrast and the regularization parameter is simple to determine. After the 3D PSWFs are precomputed, the remaining computational cost is due to matrix vector multiplication. To fully demonstrate the potential of the proposed method, we test full far field data generated by the fully nonlinear model with relative modeling error $\text{rel}(k) = 66.82\%$ and noise level $\delta = 0.2$. The iterative method with a fixed number of iterations $\text{pdaN} = 100$ costs more than one hour, where the proposed method only costs several seconds. Both methods are accurate in terms of the real part, as shown in Figure 6; however, the error of the iterative method is larger in the imaginary part, as can be seen in Figure 7.

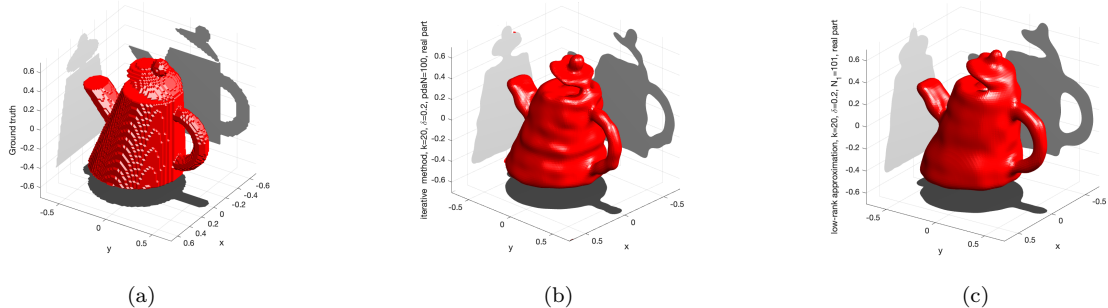


Figure 6: Reconstruction of a teapot. The first column: ground truth; the second column: the iterative method; the third column: the proposed method. Wave number $k = 20$, modeling error $\text{rel}(k) = 66.82\%$, noise level $\delta = 0.2$, and $N_1 = N_2 = 101$.

5.2.5 Reconstruction using Tikhonov regularization with H_c^s penalty

The low-rank structure provides a versatile tool for regularization by penalizing the H_c^s -norm of solutions. The difference between the low-rank approximate solution (13) and the Tikhonov regularized solution (14) is due to the additional term $\eta \chi_{m,n}^s$, and this will be a straightforward modification since the Sturm-Liouville eigenvalues $\chi_{m,n}$ have been conveniently computed according to Section 4.1. We plot in Figure 8 the reconstructions of two contrasts “cross3D” (top row) and “teapot” (bottom row) using the Tikhonov regularization

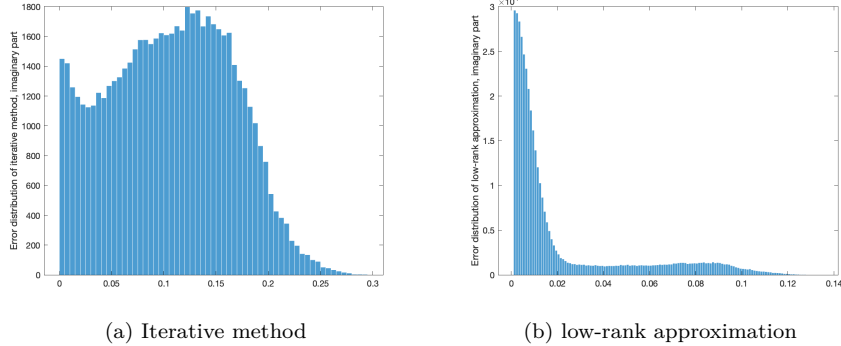


Figure 7: Reconstruction error of the imaginary part of the teapot. The imaginary part of the ground truth is zero. We plot the errors (x -axis) against 91^3 grid points (y -axis). Left: iterative method; right: low-rank approximation.

with penalty terms in $H_c^{1/4}$ (middle column) and $H_c^{1/2}$ (right column), respectively.

5.2.6 Localized imaging

Finally we demonstrate the localized imaging technique in Section 3.5. In Figure 9 the unknown contrast consists of a targeting object (teapot supported in the unit ball) surrounded by other objects, and the goal is to only image the targeting teapot. The reconstruction by the proposed low-rank structure is plotted in the middle column, and the reconstruction by the tested iterative method is given in the right column. The double orthogonality offers a localized imaging technique by manipulating the data, which filters the data by its projection onto the 3D PSWFs with dominant prolate eigenvalues. The teapot is surrounded by three complex objects in the bottom case of Figure 9, and its reconstruction by the low-rank approximation is still good while the computational cost remains the same despite the presence of surrounded complex objects. This demonstrates the potential of the low-rank structure in data processing/filtering and localized imaging techniques.

References

- [1] M. Abramowitz and I. A. Stegun. *Handbook of mathematical functions with formulas, graphs, and mathematical tables*, volume 55. US Government printing office, 1948.
- [2] T. Arens and A. Lechleiter. Indicator functions for shape reconstruction related to the linear sampling method. *SIAM Journal on Imaging Sciences*, 8(1):513–535, 2015.
- [3] L. Audibert and H. Haddar. A generalized formulation of the linear sampling method with exact characterization of targets in terms of farfield measurements. *Inverse Problems*, 30(3):035011, 2014.
- [4] L. Audibert and S. Meng. Shape and parameter identification by the linear sampling method for a restricted fourier integral operator. *Inverse Problems*, 40(9):095007, 2024.
- [5] F. Bürgel, K. S. Kazimierski, and A. Lechleiter. Algorithm 1001: Ipscatt—a matlab toolbox for the inverse medium problem in scattering. *ACM Transactions on Mathematical Software (TOMS)*, 45(4):1–20, 2019.
- [6] F. Cakoni and D. Colton. *A qualitative approach to inverse scattering theory*. Springer, 2014.
- [7] F. Cakoni, D. Colton, and P. Monk. *The linear sampling method in inverse electromagnetic scattering*. SIAM, 2011.

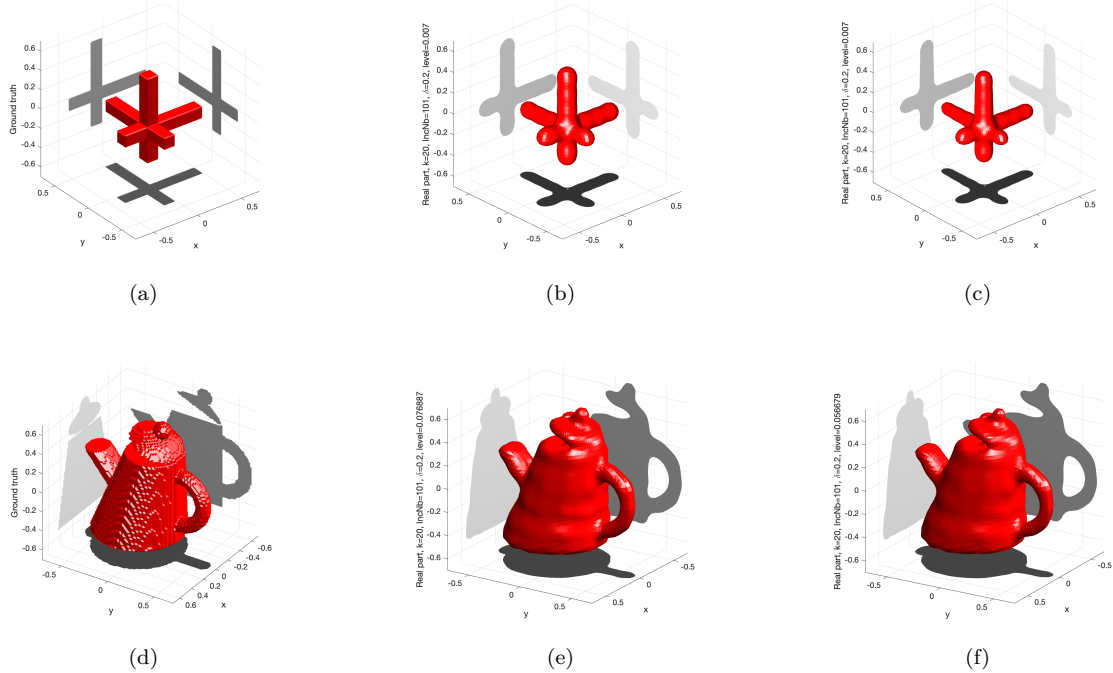


Figure 8: Reconstructions via regularization with H_c^s penalty term. The first column: ground truth; the second column: $s = \frac{1}{4}$; the third column: $s = \frac{1}{2}$. Wave number $k = 20$, noise level $\delta = 0.2$, $N_1 = N_2 = 101$, and regularization parameter $\eta = 10^{-4}$.

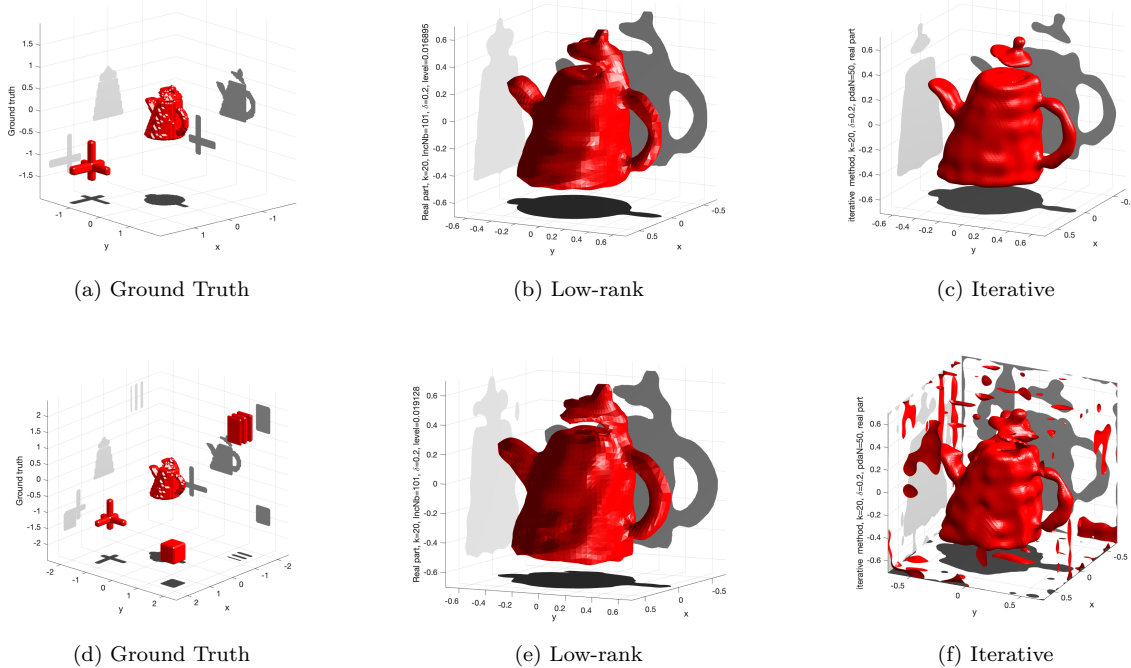


Figure 9: Imaging of a targeting teapot surrounded by other objects. Left column: ground truth; middle column: reconstruction via the low-rank structure; right column: reconstruction by the iterative method. $k = 20$, $\delta = 20\%$.

- [8] F. Cakoni, S. Meng, and Z. Zhou. On the recovery of two function-valued coefficients in the helmholtz equation for inverse scattering problems via inverse born series. *Inverse Problems*, 41(7):075004, 2025.
- [9] D. Colton and A. Kirsch. A simple method for solving inverse scattering problems in the resonance region. *Inverse problems*, 12(4):383, 1996.
- [10] D. L. Colton and R. Kress. *Inverse acoustic and electromagnetic scattering theory*, volume 93. Springer, 1998.
- [11] A. Desai, J. Ma, T. Lahivaara, and P. Monk. A neural network enhanced born approximation for inverse scattering. *arXiv preprint arXiv:2503.01596*, 2025.
- [12] Á. González. Measurement of areas on a sphere using fibonacci and latitude-longitude lattices. *Mathematical geosciences*, 42:49–64, 2010.
- [13] I. Goodfellow, Y. Bengio, A. Courville, and Y. Bengio. *Deep learning*, volume 1. MIT press Cambridge, 2016.
- [14] P. Greengard. Generalized prolate spheroidal functions: algorithms and analysis. *Pure and Applied Analysis*, 6(3):789–833, 2024.
- [15] R. Griesmaier. Multi-frequency orthogonality sampling for inverse obstacle scattering problems. *Inverse Problems*, 27(8):085005, 2011.
- [16] I. Harris and D.-L. Nguyen. Orthogonality sampling method for the electromagnetic inverse scattering problem. *SIAM Journal on Scientific Computing*, 42(3):B722–B737, 2020.
- [17] M. Isaev and R. G. Novikov. Reconstruction from the fourier transform on the ball via prolate spheroidal wave functions. *Journal de Mathématiques Pures et Appliquées*, 163:318–333, 2022.
- [18] K. Ito, B. Jin, and J. Zou. A direct sampling method to an inverse medium scattering problem. *Inverse Problems*, 28(2):025003, 2012.
- [19] Y. Khoo and L. Ying. Switchnet: a neural network model for forward and inverse scattering problems. *SIAM Journal on Scientific Computing*, 41(5):A3182–A3201, 2019.
- [20] A. Kirsch. Characterization of the shape of a scattering obstacle using the spectral data of the far field operator. *Inverse problems*, 14(6):1489, 1998.
- [21] A. Kirsch. Remarks on the born approximation and the factorization method. *Applicable Analysis*, 96(1):70–84, 2017.
- [22] A. Kirsch and N. Grinberg. *The factorization method for inverse problems*, volume 36. OUP Oxford, 2007.
- [23] K. Li, B. Zhang, and H. Zhang. Reconstruction of inhomogeneous media by an iteration algorithm with a learned projector. *Inverse Problems*, 40(7):075008, 2024.
- [24] J. Liu and J. Sun. Extended sampling method in inverse scattering. *Inverse Problems*, 34(8):085007, 2018.
- [25] X. Liu, S. Meng, and B. Zhang. Modified sampling method with near field measurements. *SIAM Journal on Applied Mathematics*, 82(1):244–266, 2022.
- [26] Y. Liu, Z. Wu, J. Sun, and Z. Zhang. Deterministic-statistical approach for an inverse acoustic source problem using multiple frequency limited aperture data. *Inverse Problems and Imaging*, 17(6):1329–1345, 2022.
- [27] W. C. H. McLean. *Strongly elliptic systems and boundary integral equations*. Cambridge university press, 2000.

- [28] S. Meng. Data-driven basis for reconstructing the contrast in inverse scattering: Picard criterion, regularity, regularization, and stability. *SIAM Journal on Applied Mathematics*, 83(5):2003–2026, 2023.
- [29] S. Meng and B. Zhang. A kernel machine learning for inverse source and scattering problems. *SIAM Journal on Numerical Analysis*, 62(3):1443–1464, 2024.
- [30] S. Moskow and J. C. Schotland. Convergence and stability of the inverse scattering series for diffuse waves. *Inverse Problems*, 24(6):065005, 2008.
- [31] A. Osipov, V. Rokhlin, and H. Xiao. Prolate spheroidal wave functions of order zero. *Springer Ser. Appl. Math. Sci*, 187, 2013.
- [32] R. Potthast. A study on orthogonality sampling. *Inverse Problems*, 26(7):074015, 2010.
- [33] D. Slepian. Prolate spheroidal wave functions, fourier analysis and uncertainty—iv: extensions to many dimensions; generalized prolate spheroidal functions. *Bell System Technical Journal*, 43(6):3009–3057, 1964.
- [34] D. Slepian and H. O. Pollak. Prolate spheroidal wave functions, fourier analysis and uncertainty—i. *Bell System Technical Journal*, 40(1):43–63, 1961.
- [35] S. Sun and G. S. Alberti. The learned range test method for the inverse inclusion problem. *SIAM Journal on Applied Mathematics*, 2025.
- [36] V. Vapnik. Support-vector networks. *Machine learning*, 20:273–297, 1995.
- [37] J. Zhang, H. Li, L.-L. Wang, and Z. Zhang. Ball prolate spheroidal wave functions in arbitrary dimensions. *Applied and Computational Harmonic Analysis*, 48(2):539–569, 2020.
- [38] Y. Zhou, L. Audibert, S. Meng, and B. Zhang. Exploring low-rank structure for an inverse scattering problem with far-field data. *SIAM Journal on Applied Mathematics*, 86(1):179–205, 2026.
- [39] Z. Zhou. On the recovery of two function-valued coefficients in the helmholtz equation for inverse scattering problems via neural networks. *Advances in Computational Mathematics*, 51(1):12, 2025.